High-yield carbon derived from commercial phenol–formaldehyde resin for broadband microwave absorption by balancing conductivity and polarization loss

Shi, Y; Li, X; Liu, Qiuyun; Zhang, C; Guo, W; Tian, K; Elias, Rob; Wang, H

Journal of Materials Science

DOI:
10.1007/s10853-023-08465-9

E-pub ahead of print: 19/04/2023

Peer reviewed version

High-yield carbon derived from commercial phenol-formaldehyde resin for broadband microwave absorption by balancing conductivity and polarization loss

Yuning Shi[1], Xueai Li[1,], Qiuyun Liu[2], Can Zhang[3], Wanchun Guo[1], Kesong Tian[1], Robert Elias[2], and Haiyan Wang [1,]**

[1]Hebei Key Laboratory of Heavy Metal Deep-Remediation in Water and Resource Reuse, State Key Laboratory of Metastable Materials Science and Technology, School of Environmental and Chemical Engineering, Yanshan University, Qinhuangdao, Hebei 066004, China

[2]The BioComposites Centre, Bangor University, Bangor, LL57 2UW, UK

[3]School of Materials Science and Engineering, Harbin Institute of Technology, Harbin 150001, P.R. China

E-mail: lixueai@ysu.edu.cn, hywang@ysu.edu.cn

ABSTRACT

Lightweight and chemically stable carbon are widely applied as attractive microwave absorption materials (MAMs). However, the effective response bandwidth of pure carbonaceous MAMs is limited due to the imbalance between conductivity and polarization loss. Herein, carbon with a large number of amorphous/nanocrystalline uneven phase interfaces prepared from commercial phenol-formaldehyde resin (PF) through simple anoxic carbonization exhibited excellent microwave absorption performance by balancing conductivity and polarization loss. Benefiting from the modification of the carbon nanocrystalline, a suitable electrical conductivity is obtained with a large number of amorphous/nanocrystalline uneven phase interfaces, allowing more incident microwaves to be lost. Thus, PF-650 exhibits a strong reflection loss of −59.62 dB and a broadband effective microwave absorption of 6.32

GHz at 2.35 mm. In contrast to typical carbonaceous MAMs with multiple chemical compositions and complicated microstructures, this work provides a promising approach to the preparation of highly efficient and yielding carbonaceous materials for practical applications.

Keywords: Broadband response, Polarization loss, Electrical conductivity, High-yield carbon, Commercial Phenol-formaldehyde resin

Introduction

Electromagnetic radiation, which is hazardous to human health and the employment of precise equipment, has become a hotspot issue that needs to be dealt with urgently due to the rapid expansion of electromagnetic communications[1–3]. The application of microwave absorption materials (MAMs) is an effective solution for completely resolving the problem of electromagnetic radiation[4]. In practical applications, excellent MAMs with a broad effective bandwidth at thin thickness are desired [5, 6]. As candidates, carbonaceous materials such as graphene[7–9], carbon black[10, 11], carbon nanotubes[12–14] are commonly utilized for microwave attenuation because of their excellent intrinsic characteristics as light weight, good thermal stability, and corrosion resistance[15, 16]. However, the aforementioned graphitic carbon materials in general have high electrical conductivity, which can lead to impedance mismatch so that more electromagnetic waves are reflected. Therefore, it is difficult for pure carbon materials to meet good impedance matching and electromagnetic wave attenuation synchronously.

Amorphous carbon, as its name implies, has no specific shape or periodic

structure and is classified as a material without long-range crystalline order, consisting of sp^2 and sp^3 hybridized carbon[17]. As a representative amorphous carbon material, phenol-formaldehyde resin (PF) derived carbon is a promising candidate to break through the above bottleneck. Initially, due to its highly disordered chemical structure and large number of defects, it has a relatively weak electrical conductivity when compared to graphitic carbon materials, making it difficult to form a conductive network to prevent electromagnetic waves from entering the material; more specifically, the presence of a large number of amorphous/nanocrystalline uneven phase interfaces can increase the interfacial polarization loss of the material. It is common for the amorphous carbon to be prepared by calcination of precursors. In the previous studies, Fan et al.[18] achieved an effective absorption bandwidth (EAB) of 5.73 GHz for hollow porous carbon spheres prepared by carbonization at 700 °C using PF as a precursor. The red blood cell like-mesoporous carbon hollow microspheres derived from PF prepared by Xu et al.[19] at 650 °C carbonization reached a reflection loss (RL) of -59.7 dB and an EAB of 3.4 GHz. Various previous studies have demonstrated that PF derived carbon materials may achieve impedance matching while maintaining attenuation capability by modifying the carbon structure with the carbonization temperature as a variable. However, the sophisticated structure and components prevent us from evaluating whether the inherent qualities of PF or the sophisticated structure are the most influential on the microwave absorption properties of PF derived carbon. Meanwhile, sophisticated structural control is known to be challenging to implement in industrial production, posing a severe obstacle to

further industrialization of many reported absorbers[20]. Therefore, it is essential to seek a facile, large-scale, high-yield, and stable method for the preparation of PF derived amorphous carbon without representative structures for practical applications.

In this study, commercial PF was used as a precursor to obtain carbonaceous materials with tunable uneven phase interfaces and electrical conductivity at a high carbon yield of 58% by one-step carbonization. The tunable amorphous/nanocrystalline uneven phase interfaces and suitable electrical conductivity provide a significant balance between polarization and conductivity loss for achieving broadband response. By altering the carbonization temperature so as to change the chemical microstructure and graphitization of the derived carbon material, the PF derived amorphous carbon can reach the ultra-wide bandwidth of 6.32 GHz covering the whole Ku-band with a thickness of 2.35 mm. This work provides a functional low-cost carbon material for broadband microwave absorption by simple carbonization using commercial products as precursors, which greatly reduces the difficulty of industrializing the absorber.

Results and Discussion

The functional groups included in the commercial PF were detected via infrared testing. As shown in Fig. S1a (Supporting Information), the absorption peak caused by the variable angle vibration of the phenolic hydroxyl group and the antisymmetric stretching vibration of the aryl ether bond, which is the main characteristic peak of the PF[21] can be observed at 1230 cm^{-1}. The stretching vibrations of functional groups, such as hydroxyl, methylene, and aromatic rings, create the other absorption peaks,

demonstrating that the commercial powder is PF[22, 23]. Also, thermogravimetric test was performed on commercial PF in oxygen atmospheres. It can be seen from Fig. S1b that the sample has been completely burned at 700 °C without any residue, proving that the commercial PF is basically free of inorganic impurities.

In order to implement the modulation of electrical conductivity and investigate the carbonization temperature for this study, thermogravimetric analysis was carried on commercial PF. Fig. 1a shows the thermogravimetry (TG) and the derivative thermogravimetry (DTG) curves of PF from 10 °C to 1200 °C under nitrogen atmosphere at a heating rate of 10 °C/min. The dominant pyrolysis temperature range for commercial PF can be seen in the graph from 200 °C to 800 °C, where the loss of the material is approximately 37.8%. The weight loss was about 4.05% at temperatures below 200 °C, which was attributed to absorbed water and unreacted oligomers, meanwhile the PF basically stopped losing weight at temperatures above 800 °C, indicating that it was completely carbonized after 800 °C. According to previous studies[22, 24, 25], the pyrolysis process from 200 °C to 800 °C can be divided into three stages. In the third stage, the C-H bond in the aromatic ring is broken to form H_2, and PF is gradually transformed into amorphous carbon through the polycyclic reaction. Based on this, four temperatures were selected for the carbonization of PF: 600 °C, 650 °C, 700 °C and 800 °C. The caron yield of commercial PF was calculated to be up to 58%. Table S1 lists the carbon yields of several typical carbon precursors. Obviously, commercial PF has the highest carbon yield, indicating that it is a superior precursor.

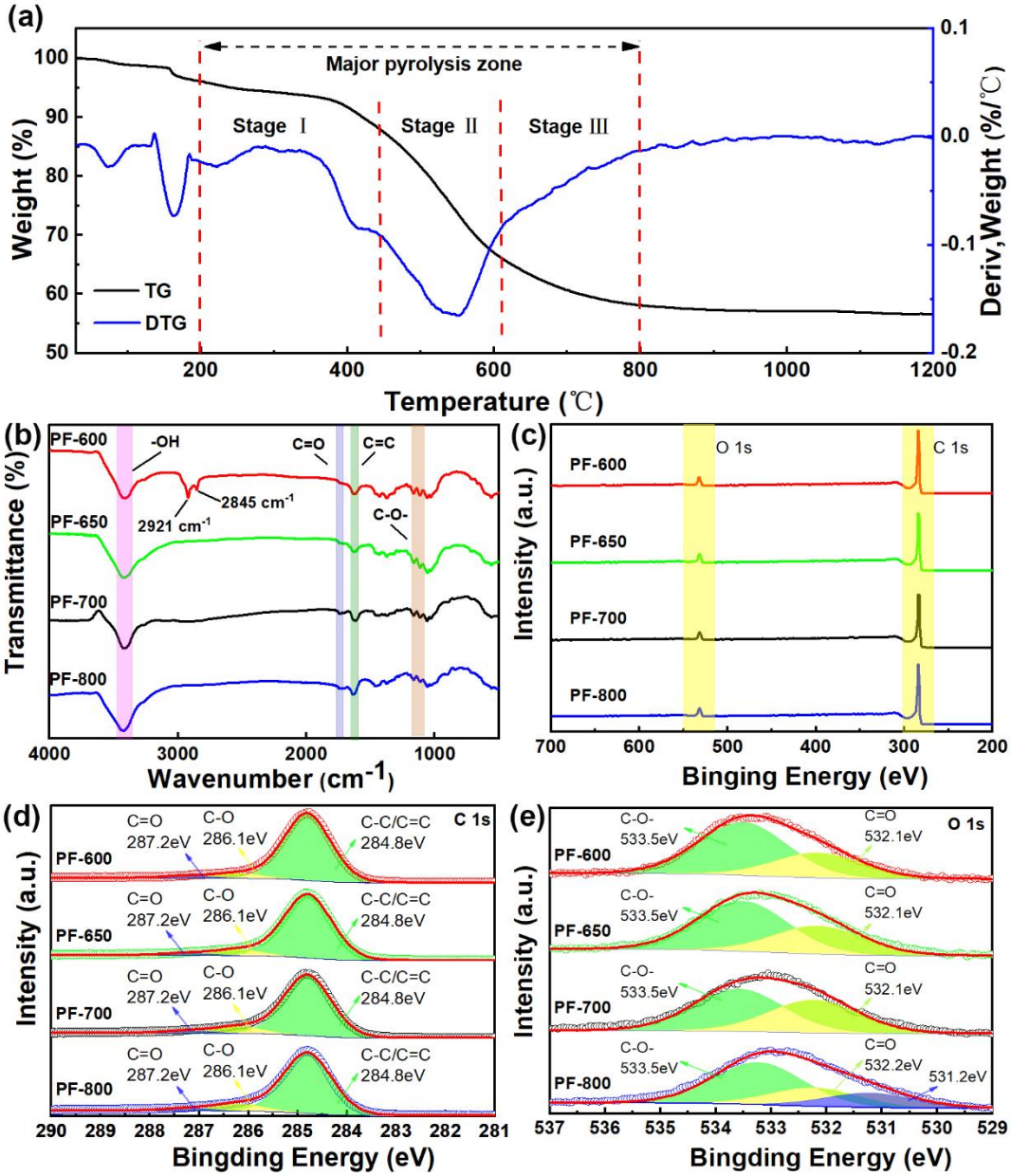

Figure 1 a TG and DTG curves of PF in the N_2 atomsphere. **b** FTIR spectrum, **c** XPS spectrum, **d** high resolution C 1s XPS spectrum, **e** high resolution O 1s XPS spectrum of PF-600/650/700/800

The microstructure of the four samples were observed through TEM. As can be seen from Fig. S2(Supporting Information), all four samples exhibit a clumpy morphology with a smooth surface, and no significant pore structure is observed. As shown in Fig. S3(Supporting Information), nitrogen adsorption and desorption isotherms and pore size distributions calculated were used to characterize the pore structure of the material. The surface area of PF-600/650/700/800 with the presence

of a large number of micropores around 0.6 nm were 609.3 $m^2 \cdot g^{-1}$,577.7 $m^2 \cdot g^{-1}$,612.7 $m^2 \cdot g^{-1}$, 616.6 $m^2 \cdot g^{-1}$, respectively. It can be seen that within the temperature range studied, the influence of carbonization temperature on the surface area and pore structure of the carbon can be ignored. The constant escape of pyrolytic gas during the carbonization process is the reason of the high surface area and large quantity of micropores.

Infrared tests were carried out to investigate the chemical structure of the resultant samples, with the results displayed in Fig. 1b. The broad peak present around 3400 cm^{-1} is attributed to the stretching vibration of -OH, which may come from the moisture in the sample but not from the phenolic hydroxyl group present in the PF itself. The peak around 1737 cm^{-1} comes from the stretching vibration of C=O, while the peak at 1629 cm^{-1} comes from the stretching vibration of the C=C bond in the aromatic ring, and the two peaks at 1117 cm^{-1} and 1168 cm^{-1} may be due to the stretching vibration of C-O-[26, 27]. All three peaks are present in the samples at four different carbonization temperatures which belonged to the residual functional groups during the carbonization of commercial PF. However, only PF-600 has a stretching vibration peak of C-H on aliphatic group at 2921 cm^{-1} and 2845 cm^{-1}[28]. This indicates that the original resin structure of the PF disappears and gradually starts to graphitize at the carbonization temperature above 600 °C, which is consistent with the results of thermogravimetric analysis.

To further demonstrate the chemical elements and surface electronic states, XPS tests were performed on the samples. The total spectrum of XPS in Fig. 1c reveals

that all samples contain two characteristic peaks C 1s and O 1s, which together with the results of the organic elemental analysis (Fig. S4, Supporting Information) demonstrate that the four samples contain only three elements C, H and O. Fig. 1d shows the high resolution C 1s XPS spectrum of the sample with three peaks at 284.8 eV, 286.1 eV, 287.2 eV corresponding to C-C/C=C, C-O, C=O, meanwhile Fig. 1e presents the high resolution O1S XPS spectrum of the sample with two peaks at 532.1 eV,533.5 eV relating to C=O, C-O- respectively[29, 30]. From Table S2, there is no obvious difference in the concentration of C,O atoms on the surface of the four samples. However, it is noteworthy that the results from the organic element analysis (Fig. S4, Supporting Information) show a large variation among four samples which indicates that the elemental distribution of the prepared material is not uniform.

XRD was employed to examine the crystal structure of the PF derived material, as shown in Fig. 2a. The four samples all have two amorphous diffraction peaks at around 23° and 44°, representing the (002) and (101) crystal plane of graphitic carbon, correspondingly[31]. As the carbonization temperature increases, the first peaks of the samples have a process of moving from a low angle to a high angle implying the gradual growth of nanocrystallines. R=B/A is an empirical parameter defined by Liu[32], where a smaller R represents a larger percentage of the single layers in carbonaceous materials[33]. The empirical parameters of four samples are 2.69, 2.11, 2.02, 2.13 (Fig. 2c, S5a, S5b, S5c), correspondingly. The non-monotonic increase in R could be owing to the gradual development of more and more single layer graphite-like structures as the carbonization temperature rises; however, as the

temperature exceeds 700 °C, the single layer structures begin to stack and form multilayer structures. This proves that the orderliness of the samples gradually increases with increasing carbonization temperature which can also be corroborated by the analysis of Raman spectra.

Two distinctive peaks of carbon features at both 1340 cm^{-1} and 1590 cm^{-1} can be observed in the Raman spectra as shown in Fig. 2c, where the peak at 1340 cm^{-1} is referred to as D peak associated with disordered sp^3 hybridized carbon atoms and defects, and the peak at 1590 cm^{-1} is referred to as G peak from the Raman scattering of graphitic carbon sp^2 hybridized carbon atoms[34, 35]. For amorphous carbon, the ratio of D-peak to G-peak intensity is directly proportional to the plane size of the microcrystal[36]. The I_D/I_G keeps improving as the carbonization temperature increases, which proves that the microcrystalline planar size of the sample then grows and the orderliness is continuously enhanced. The I_D/I_G change during the transition from amorphous carbon to graphitic carbon is divided into two stages, according to the models proposed by Ferrari and Robertson[37], with I_D/I_G increasing when amorphous carbon is converted to nanocrystalline graphitic carbon and I_D/I_G decreasing during the subsequent nanocrystalline graphitic to graphitic transition. It is apparent that the commercial PF is undergoing a transition from amorphous carbon to nanocrystalline graphite in the temperature range of 600 ℃ -800 ℃. Further fitting and deconvolution of the Raman spectrum into four peaks[38] is shown in Fig. 2d. The R_1 peak at 1180 cm^{-1} is associated with sp^3 or sp^2–sp^3 bonding[39, 40] and the R_2 peak at 1550 cm^{-1} is an amorphous carbon band attributed to a wide range of carbon

structures such as off-plane defects, organic molecules or functional groups with sp^2 bonding[38]. The absence of R_2 peaks only in the amorphous carbon structure was present in all four samples (Fig. S5d, S5e, S5f) indicating that the four samples were amorphous carbon in agreement with the previous analysis.

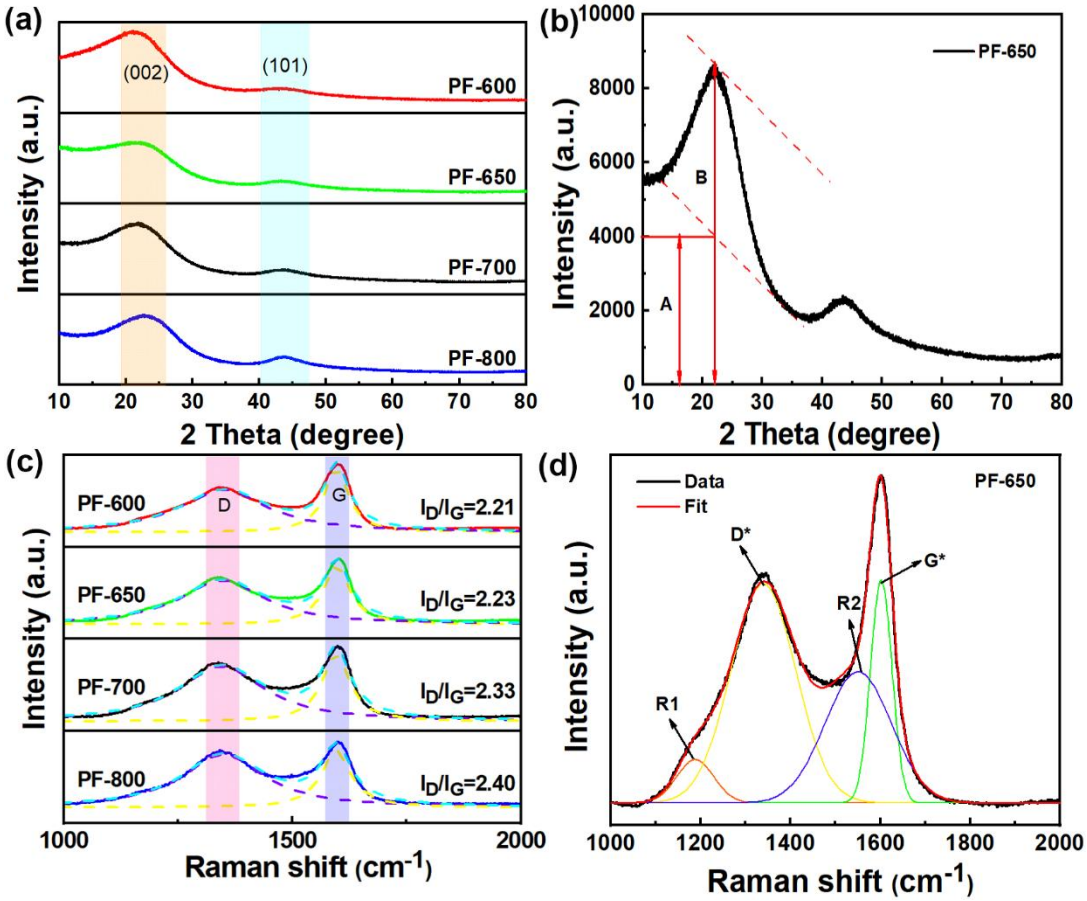

Figure 2 a XRD patterns, **b** XRD pattern of the definition of the parameter R for PF-650, **c** Raman patterns, **d** Deconvoluted Raman spectra for PF-650

Hence, based on the above test results, the microchemical structure of the samples carbonized at 600-800°C was summarized. PF-600 exhibits a highly disordered state, with only a few aromatic rings cross-linked together to form a graphite-like carbon structure. When the carbonization temperature was raised to 650 °C, PF-650 microchemical structure changed dramatically, tending to be ordered while some semi-graphite micro-domain are formed. Then, the single layer

graphite-like carbon structures begin to stack and the semi-graphite micro-domain start to transform into graphite micro-domain in PF-700. Then, multilayer graphite-like structures are formed with the fusion of graphite microdomains in contact in PF-800.

It is widely known that the pyrolysis temperature exerts a significant effect on the electrical conductivity of polymers[41]. The four-probe technique was used to test the electrical conductivity of the samples. From Fig. 3a, it is obvious that PF-600 is almost non-conductive, which is due to the fact that it still has some of the original chemical structure of the PF and the electrons are in a bound state, yet the electrical conductivity of PF-650 increases significantly due to the formation of a conductive network in some regions caused by the aromatic ring rearrangement. The electrical conductivity elevates markedly due to the growing developed carbon nanocrystalline with an increase in carbonization temperature.

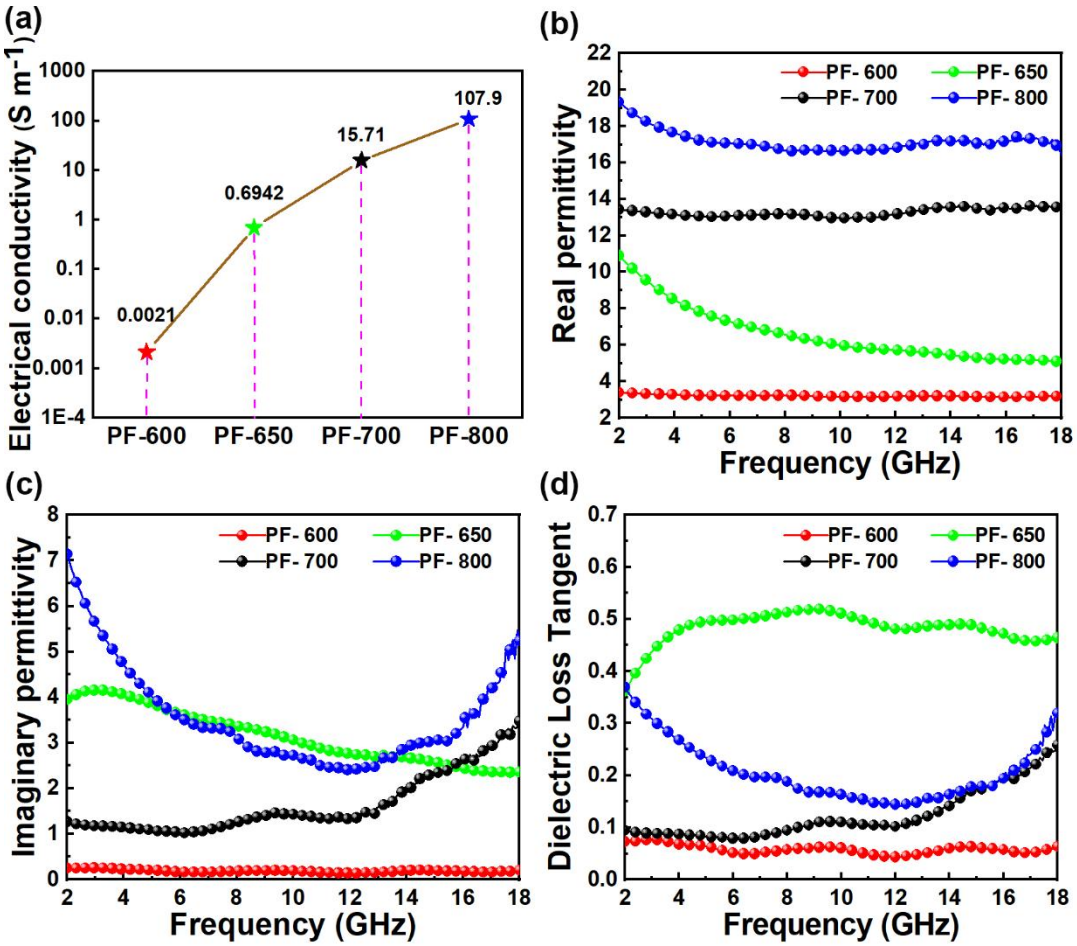

Figure 3 a Electrical conductivity of PF-600/650/700/800, Frequency-dependent complex permittivity: **b** real part, **c** imaginary part, **d** dielectric loss tangent

The microwave absorption of the material is evaluated by the complex permittivity and complex permeability. Since the carbon materials are typically non-magnetic, the influence of complex permeability as shown in Fig. S6a, b can be basically ignored. We only need to focus on the variation of the complex permittivity ($\varepsilon_r = \varepsilon' - j\varepsilon''$) of the materials, where the real part (ε') is related to the material's ability to store electrical energy and the imaginary part (ε'') is linked to the material's ability to loss electrical energy[42]. It can be seen from Fig. 3b, with the increase of the carbonization temperature, the real part of the complex dielectric permittivity is rising which may be due to more free electrons being produced. On the contrary, there is an interesting phenomenon that the imaginary part doesn't show the same trend as

the real part in which it can be seen from Fig. 3c that the imaginary part of PF-650 is obviously higher than PF-700. According to the Debye theory, the ε'' can be divided into two parts: polarization loss and conductive loss[43], as shown in eq. 3:

$$\varepsilon'' = \varepsilon''_{\rho} + \varepsilon''_{c} = (\varepsilon_s - \varepsilon_\infty)\frac{2\pi f\tau}{1+(2\pi f)^2\tau^2} + \frac{\sigma}{2\pi f\varepsilon_0} \qquad (3)$$

According to eq. 3, electrical conductivity and conductivity loss have a positive correlation. Hence, due to the increasing of electrical conductivity as shown in Fig. 3a, the conductivity loss tends to rise with the gradual growth of nanocrystalline. The Cole-Cole cure with ε'' as the vertical coordinate and ε' as the horizontal coordinate was potted according to eq. 4, where each Cole-Cole semicircle represents a Debye polarization process[44, 45], as shown in Fig. S7

$$(\varepsilon' - \frac{\varepsilon_s+\varepsilon_\infty}{2})^2 + (\varepsilon'')^2 = (\frac{\varepsilon_s-\varepsilon_\infty}{2})^2 \qquad (4)$$

Clearly, Cole-Cole semicircles are present in all four samples, stating the evidence of dipole polarization caused by heteroatoms and defects[46]. But only PF-800 has a long trailing tail, which represents conductivity loss due to the larger conductivity of the PF-800. In addition, with the gradual growth of nanocrystalline, a transition from amorphous to graphitized carbon is occurring. A large number of amorphous/nanocrystalline uneven phase interfaces generate interfacial polarization losses. As the carbonization temperature rises, the increasing of PF derived carbon material's electrical conductivity enhances conductivity loss, while the reduction of defects, heteroatoms, and uneven phase interfaces decreases the dipole and interfacial polarization loss. Thus, the inconsistent changes between conductivity loss and polarization loss of four samples cause the trend in Fig. 3b. The electrical

conductivity and uneven phase interfaces of phenol-formaldehyede resin derived carbon which affects the electromagnetic response is inherited from the suitable degree of cross-linking of phenol-formaldehyede resin. In general, the dielectric loss tangent ($tha\delta_{\varepsilon} = \frac{\varepsilon''}{\varepsilon'}$)[47] in MAMs is used to evaluate the loss capability of material to microwaves, where the greater the loss angle, the stronger the loss capability. As presented in Fig. 3c, PF-650 exhibits a far superior loss capacity than the other samples due to the balance between conductivity loss and polarization loss. Fig. S8 shows the impedance matching value at the optimum effective absorption bandwidth condition of the samples. Clearly, the Z values of PF-650 are close to 1 over most frequency range, indicating its better impedance matching than those of other samples.

According to the transmission line theory[48], the microwave absorbing capability of samples were evaluated in the 2-18GHz. The 3D maps of all samples were displayed in Fig. 4a, b, c, d. Apparently, the PF-600 samples show a weakly microwave absorbing performance in which at all thicknesses the reflection loss (RL) is more than -10 dB as can be seen in Figure 3a. However, when the carbonization temperature was up to 650 ℃, the microwave absorbing capability has drastically increasing. The minimum value of RL (RL_{min}) was -59.62 dB and the EAB in which the RL value below -10 dB can be up to 6.32 GHz at 2.35 mm. The samples under 700 ℃ and 800 ℃ carbonization temperature have similarity EAB values of 2.24 GHz at 1.29 mm and 2.32 GHz at 1.17 mm. Nevertheless, the RL_{min} value of PF-800 is stronger than PF-700. On the whole, the sample PF-650 has an outstanding

performance which is far beyond the thin, lightweight, broad and strong RL standard. The RL_{min} value of PF-800 can be up to -62.43 dB, as shown in Fig. 4e, the thickness reached 5.0 mm, which cannot meet the requirements of practical application. From an industrial point of view, the target we pursue are on one hand broadband response to ensure its microwave absorption performance, and on the other hand a lower carbon material carbonization temperature to reduce costs. Fig. 4g compares the carbonization temperature and the EAB of PF-650 with other carbon absorbers.[18, 19, 43, 49–55] As expected, PF-650 with suitable electrical conductivity and uneven phase interfaces achieves a 6.32 GHz broad EAB at a relatively low carbonization temperature.

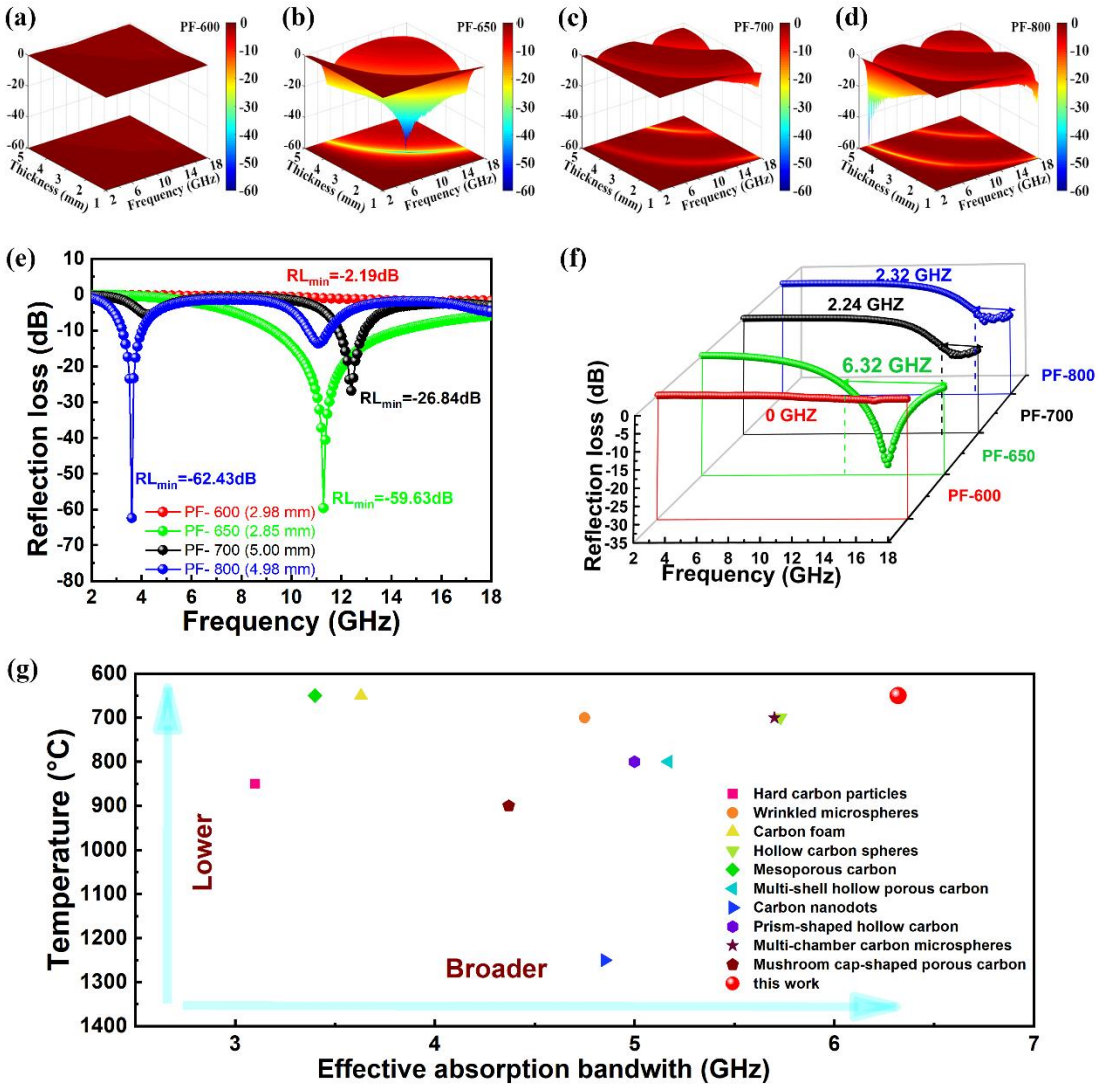

Figure 4 3D maps of RL-f-d of **a** PF-600, **b** PF-650, **c** PF-700, **d** PF-800. **e** Minimum reflection loss (RL_{min}) and **f** maximum effective absorption bandwidth (EAB_{max}) values of the PF-600/650/700/800. **g** Microwave absorption properties and carbonization temperature comparison (2−18 GHz) of PF-650 with other reported carbon absorbers

Combined with the above analysis, the main loss mechanism of PF-650 can be summarized in the following three aspects indicated in Fig. 5. (1) Charges gather at the interfaces of uneven-phase media with variable electrical conductivities where nanocrystalline carbon is in contact with amorphous carbon to induce interfacial polarization effects. (2) The residual polar functional groups in the carbonization process can be served as polarization centers for dipole polarization loss of

electromagnetic waves, while the irregular carbon structure also has defects causing vacancy defect polarization.[56] (3) The conductivity loss is achieved on some graphitized carbon by electron hopping and migrating.[57]

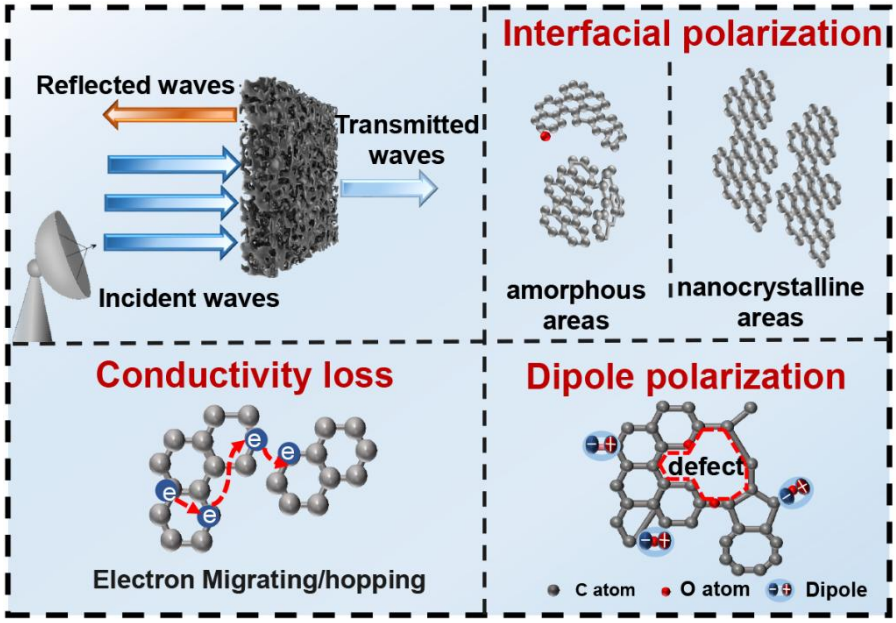

Figure 5 Schematic diagrams of the dominant electromagnetic energy loss mechanisms of PF-650

Conclusion

In this study, a facile method was used to carbonize the commercial PF with a high yield of 58%. XRD, Raman, XPS, and other testing methods have been used to investigate and discuss the impact of carbonization temperature on the amorphous/nanocrystalline uneven phase interfaces and electrical conductivity of PF derived carbon. Due to the modulation of carbon nanocrystalline, the amorphous/nanocrystalline uneven phase interfaces of PF derived carbon decreases with the graphitization degree increasing as the carbonization temperature increases. Therefore, through the synergistic effect of attenuation properties and matching properties, PF-650 shows outstanding microwave absorption performance with a RL_{min} of -59.6 dB and an EAB of 6.32 GHz. This work shows the potential of

amorphous carbon in balancing conductivity and polarization loss while also providing a carbon absorber with simple construction and outstanding performance.

Experimental Section

Synthesis Procedures. Commercial PF was supplied by Zhengzhou (China). The PF powder was pyrolyzed to the required temperature under the Ar atmosphere and maintained for 4h in the desired temperature. The following samples are named as PF-T, in which T means carbonization temperature.

Characterization. The microstructural images were obtained by transmission electron microscopy (TEM, HITACHI HT-700). The thermogravimetric analysis (TG, NETZSCH STA449FS) was employed to research the thermal behavior of commercial PF. X-ray diffraction (XRD, Rigaku D-max-2500/PC) spectra and Raman spectra (He-Ne Renishaw in via) were collected to study the graphitization degree and defect of the samples. Fourier-transform infrared spectroscopy (FTIR, NICOLET iS10) and X-ray photoelectron spectroscopy (XPS, ESCALAB 250Xi) test were taken to analyze the chemical bond and the atom composition of the samples, respectively. A four-probe semiconductor resistivity of the powder tester (ST-2722, Suzhou Jingge) was carried out to record the electrical conductivity. C/H mass ratio were calculated through the test result by organic elemental analyzer (Elemantar: Vario EL cube) Nitrogen adsorption–desorption curves and pore-size distributions were obtained by nitrogen adsorption and desorption analyzer (ASAP 2460). An Agilent N5234A vector network was used to record the relative complex permittivity and permeability

in the frequency 2GHz to18GHz. Based on the transmission line theory, the reflection loss (RL) was calculated. The formula as follow:

$$RL = 20\log|\frac{Z_{in}-Z_0}{Z_{in}+Z_0}| \quad (1)$$

$$Z_{in} = Z_0\sqrt{\frac{\mu_r}{\varepsilon_r}}tanh\left[\frac{j2\pi ft}{c}\sqrt{\mu_r\varepsilon_r}\right] \quad (2)$$

In which Z_{in} is the input impedance of the absorber, f, t and c represent the incident electromagnetic wave frequency, thickness of composites and velocity of light.

Acknowledgements

This work was financially supported by National Natural Science Foundation of China (51802278), Natural Science Foundation of Hebei Province (No. E2022203082, B2021203012), and Science and Technology Project of Higher Education in Hebei Province (QN2021140).

Conflict of Interest

The authors declare no conflict of interest.

Data Availability Statement

The data that support the findings of this study are available from the corresponding author upon reasonable request.

Supporting Information

FTIR spectrum and TG curve of PF of PF, the TEM image of PF-600/650/700/800, C/H and C/O mass ratio of PF-600/650/700/800, XRD pattern of the definition of the parameter R and deconvoluted Raman spectra for PF-600/700/800, Frequency-dependent complex permeability: real part, imaginary part, attenuation constant α and Cole−Cole plots of PF-600/650/700/800, nitrogen adsorption-desorption isotherms and pore size distributions calculated result of

PF-600/650/700/800, the impedance matching value at the optimum effective absorption bandwidth condition of the PF-600/650/700/800, carbon yield of different precursors, the elementary compositions of PF-600/650/700/800.

References

1. Ren X, Gao Z, Wu G (2022) Tunable nano-effect of Cu clusters derived from MOF-on-MOF hybrids for electromagnetic wave absorption. Composites Communications 35:101292. https://doi.org/10.1016/j.coco.2022.101292

2. Ren X, Song Y, Gao Z, et al (2023) Rational manipulation of composition and construction toward Zn/Co bimetal hybrids for electromagnetic wave absorption. J Mater Sci Technol 134:254–261. https://doi.org/10.1016/j.jmst.2022.07.004

3. Zhang C, Li X, Shi Y, et al (2022) Structure Engineering of Graphene Nanocages toward High-Performance Microwave Absorption Applications. Adv Opt Mater 10:2101904. https://doi.org/10.1002/adom.202101904

4. Wang C, Ding J, Gong C, et al (2023) Hierarchical pomegranate-like MnO@N-doped carbon with enhanced conduction loss and interfacial polarization for tunable and broadband microwave absorption. J Mater Sci 58:211–229. https://doi.org/10.1007/s10853-022-08008-8

5. Ding J, Song K, Gong C, et al (2022) Design of conical hollow ZnS arrays vertically grown on carbon fibers for lightweight and broadband flexible absorbers. J Colloid Interface Sci 607:1287–1299. https://doi.org/10.1016/j.jcis.2021.08.189

6. Wang S, Li Q, Hu K, et al (2021) A facile synthesis of bare biomass derived holey carbon absorbent for microwave absorption. Applied Surface Science 544:148891. https://doi.org/10.1016/j.apsusc.2020.148891

7. Cheng Z, Wang R, Cao Y, et al (2022) Intelligent Off/On Switchable Microwave Absorption Performance of Reduced Graphene Oxide/VO_2 Composite Aerogel. Adv Funct Mater 32:2205160. https://doi.org/10.1002/adfm.202205160

8. Zhi D, Li T, Qi Z, et al (2022) Core-shell heterogeneous graphene-based aerogel microspheres for high-performance broadband microwave absorption via resonance loss and sequential attenuation. Chem Eng J 433:134496. https://doi.org/10.1016/j.cej.2022.134496

9. Huang Q, Zhao Y, Wu Y, et al (2022) A dual-band transceiver with excellent heat insulation property for microwave absorption and low infrared emissivity compatibility. Chem Eng J 446:137279. https://doi.org/10.1016/j.cej.2022.137279

10. Lei L, Yao Z, Zhou J, et al (2020) 3D printing of carbon black/polypropylene composites with excellent microwave absorption performance. Compos Sci Technol 200:108479. https://doi.org/10.1016/j.compscitech.2020.108479

11. He P, Zhang J, Xiong Y, et al (2022) Mechanochemical synthesis of core-shell carbon black@acrylic resin nanocomposites with enhanced microwave absorption. Compos Sci Technol 228:109665. https://doi.org/10.1016/j.compscitech.2022.109665

12. Wang Y-Y, Song-Yang, Sun W-J, et al (2022) Highly enhanced microwave absorption for carbon nanotube/barium ferrite composite with ultra-low carbon nanotube loading. J Mater Sci Technol 102:115–122. https://doi.org/10.1016/j.jmst.2021.06.032

13. Liu D, Yang L, Wang F, et al (2022) Hierarchical carbon nanotubes@Ni/C foams for high-performance microwave absorption. Carbon 196:867–876. https://doi.org/10.1016/j.carbon.2022.05.057

14. Zhang C, Shi Y, Li X, et al (2022) Architecture inspired structure engineering toward carbon nanotube hybrid for microwave absorption promotion. iScience 25:105203. https://doi.org/10.1016/j.isci.2022.105203

15. Tao J, Zhou J, Yao Z, et al (2021) Multi-shell hollow porous carbon nanoparticles with excellent microwave absorption properties. Carbon 172:542–555. https://doi.org/10.1016/j.carbon.2020.10.062

16. Luo J, Feng M, Dai Z, et al (2022) MoS2 wrapped MOF-derived N-doped carbon nanocomposite with wideband electromagnetic wave absorption. Nano Res. https://doi.org/10.1007/s12274-022-4411-6

17. Okwundu OS, Aniekwe EU, Nwanno CE (2018) Unlimited potentials of carbon: different structures and uses (a Review). Metall Mater Eng 24:145–171. https://doi.org/10.30544/388

18. Fan D, Wei B, Wu R, et al (2021) Dielectric control of ultralight hollow porous carbon spheres and excellent microwave absorbing properties. J Mater Sci 56:6830–6844. https://doi.org/10.1007/s10853-021-05780-x

19. Xu H, Yin X, Li M, et al (2018) Mesoporous carbon hollow microspheres with red blood cell like morphology for efficient microwave absorption at elevated temperature. Carbon 132:343–351. https://doi.org/10.1016/j.carbon.2018.02.040

20. Nan H, Luo F, Jia H, et al (2021) The effect of temperature on structure and permittivity of carbon microspheres as efficient absorbent prepared by facile and large-scale method. Carbon 185:650–659. https://doi.org/10.1016/j.carbon.2021.09.070

21. Shukla SK, Srivastava D, Srivastava K (2015) Synthesis, Spectral and Thermal Degradation Kinetics of the Epoxidized Resole Resin Derived from Cardanol. Adv Polym Technol 34:21469. https://doi.org/10.1002/adv.21469

22. Chen ZQ, Chen YF, Liu HB (2013) Study on Thermal Degradation of Phenolic Resin. Appl Mech Mater 422:24–28. https://doi.org/10.4028/www.scientific.net/AMM.422.24

23. Morterra C, Low MJD (1985) I.R. studies of carbons—VII. The pyrolysis of a phenol-formaldehyde resin. Carbon 23:525–530. https://doi.org/10.1016/0008-6223(85)90088-0

24. Chen S, Liu Z, Jiang S, Hou H (2020) Carbonization: A feasible route for reutilization of plastic wastes. Sci Total Environ 710:136250. https://doi.org/10.1016/j.scitotenv.2019.136250

25. Zheng F, Ren Z, Xu B, et al (2021) Elucidating multiple-scale reaction behaviors of phenolic resin pyrolysis via TG-FTIR and ReaxFF molecular dynamics simulations. J Anal Appl Pyrolysis 157:105222. https://doi.org/10.1016/j.jaap.2021.105222

26. Ouchi K (1966) Infra-red study of structural changes during the pyrolysis of a phenol-formaldehyde resin. Carbon 4:59–66. https://doi.org/10.1016/0008-6223(66)90009-1

27. Wang J, Jiang H, Jiang N (2009) Study on the pyrolysis of phenol-formaldehyde (PF) resin and modified PF resin. Thermochim Acta 496:136–142. https://doi.org/10.1016/j.tca.2009.07.012

28. Trick KA, Saliba TE (1995) MECHANISMS OF THE PYROLYSIS OF PHENOLIC RESIN IN A CARBON/PHENOLIC COMPOSITE. Carbon 33:1509–1515. https://doi.org/10.1016/0008-6223(95)00092-R

29. de la Puente G, Pis JJ, Menéndez JA, Grange P (1997) Thermal stability of oxygenated functions in activated carbons. J Anal Appl Pyrolysis 43:125–138. https://doi.org/10.1016/S0165-2370(97)00060-0

30. Terzyk AP (2001) The influence of activated carbon surface chemical composition on the adsorption of acetaminophen (paracetamol) in vitro Part II. TG, FTIR, and XPS analysis of carbons and the temperature dependence of adsorption kinetics at the neutral pH. Colloids Surf A 177:23–45

31. Ko T-H, Kuo W-S, Chang Y-H (2001) Microstructural changes of phenolic resin during pyrolysis. J Appl Polym Sci 81:1084–1089. https://doi.org/10.1002/app.1530

32. Xue JS, Dahn TaozhengJR (1996) MECHANISM OF LITHIUM INSERTION IN HARD CARBONS PREPARED BY PYROLYSIS OF EPOXY RESINS. Carbon 34:193–200

33. Nan H, Luo F, Jia H, et al (2022) Balancing Between Polarization and Conduction Loss toward Strong Electromagnetic Wave Absorption of Hard Carbon Particles with Morphology Heterogeneity. ACS Appl Mater Interfaces 14:19836–19846. https://doi.org/10.1021/acsami.2c01171

34. Hou Y, Quan J, Su X, et al (2021) Carbonized Silk Fiber Mat: a Flexible and Broadband Microwave Absorber, and the Length Effect. ACS Sustainable Chem Eng 9:12747–12754. https://doi.org/10.1021/acssuschemeng.1c02857

35. Gong C, Jiang J, Ding J, et al (2022) Graphene oxide supported Yolk – Shell ZnS/Ni3S4 with the adjustable air layer for high performance of electromagnetic wave absorber. J Colloid Interface Sci 617:620–632. https://doi.org/10.1016/j.jcis.2022.03.005

36. Ko T-H, Kuo W-S, Chang Y-H (2000) Raman study of the microstructure changes of phenolic resin during pyrolysis. Polym Compos 21:745–750. https://doi.org/10.1002/pc.10229

37. Ferrari AC, Robertson J (2004) Raman spectroscopy of amorphous, nanostructured, diamond–like carbon, and nanodiamond

38. Jiménez F, Mondragón F, López D (2012) Structural changes in coal chars after pressurized pyrolysis. J Anal Appl Pyrolysis 95:164–170. https://doi.org/10.1016/j.jaap.2012.02.003

39. Zaida A, Bar-Ziv E, Radovic LR, Lee Y-J (2007) Further development of Raman Microprobe spectroscopy for characterization of char reactivity. Proc Combust Inst 31:1881–1887. https://doi.org/10.1016/j.proci.2006.07.011

40. Chabalala VP, Wagner N, Potgieter-Vermaak S (2011) Investigation into the evolution of char structure using Raman spectroscopy in conjunction with coal petrography; Part 1. Fuel Process Technol 92:750–756. https://doi.org/10.1016/j.fuproc.2010.09.006

41. Bücker W (1973) Preparation and DC conductivity of an amorphous organic semiconducting system. J Non-Cryst Solids 12:115–128. https://doi.org/10.1016/0022-3093(73)90058-6

42. Yang W, Li R, Jiang B, et al (2020) Production of hierarchical porous carbon nanosheets from cheap petroleum asphalt toward lightweight and high-performance electromagnetic wave absorbents. Carbon 166:218–226. https://doi.org/10.1016/j.carbon.2020.05.043

43. Tao J, Zhou J, Yao Z, et al (2021) Multi-shell hollow porous carbon nanoparticles with excellent microwave absorption properties. Carbon 172:542–555. https://doi.org/10.1016/j.carbon.2020.10.062

44. Ye X, Chen Z, Li M, et al (2019) Microstructure and Microwave Absorption Performance Variation of SiC/C Foam at Different Elevated-Temperature Heat Treatment. ACS Sustainable Chem Eng 7:18395–18404. https://doi.org/10.1021/acssuschemeng.9b04062

45. Wu Y, Tan S, Zhao Y, et al (2023) Broadband multispectral compatible absorbers for

radar, infrared and visible stealth application. Prog Mater Sci 135:101088. https://doi.org/10.1016/j.pmatsci.2023.101088

46. Gong C, Ding J, Wang C, et al (2023) Defect-induced dipole polarization engineering of electromagnetic wave absorbers: Insights and perspectives. Composites Part B: Engineering 252:110479. https://doi.org/10.1016/j.compositesb.2022.110479

47. Mu Z, Wei G, Zhang H, et al (2022) The dielectric behavior and efficient microwave absorption of doped nanoscale LaMnO3 at elevated temperature. Nano Res 15:7731–7741. https://doi.org/10.1007/s12274-022-4500-6

48. Wang J, Huyan Y, Yang Z, et al (2019) Tubular carbon nanofibers: Synthesis, characterization and applications in microwave absorption. Carbon 152:255–266. https://doi.org/10.1016/j.carbon.2019.06.048

49. Nan H, Luo F, Jia H, et al (2022) Balancing Between Polarization and Conduction Loss toward Strong Electromagnetic Wave Absorption of Hard Carbon Particles with Morphology Heterogeneity. ACS Appl Mater Interfaces 14:19836–19846. https://doi.org/10.1021/acsami.2c01171

50. Deng W, Li T, Li H, et al (2022) Controllable graphitization degree of carbon foam bulk toward electromagnetic wave attenuation loss behavior. J Colloid Interface Sci 618:129–140. https://doi.org/10.1016/j.jcis.2022.03.071

51. Xu J, Cui Y, Wang J, et al (2020) Fabrication of wrinkled carbon microspheres and the effect of surface roughness on the microwave absorbing properties. Chem Eng J 401:126027. https://doi.org/10.1016/j.cej.2020.126027

52. Liu D, Du Y, Wang F, et al (2020) MOFs-derived multi-chamber carbon microspheres with enhanced microwave absorption. Carbon 157:478–485. https://doi.org/10.1016/j.carbon.2019.10.056

53. Yang W, Yang X, Hu J, et al (2021) Mushroom cap-shaped porous carbon particles with excellent microwave absorption properties. Appl Surf Sci 564:150437. https://doi.org/10.1016/j.apsusc.2021.150437

54. Li X, Yu L, Zhao W, et al (2020) Prism-shaped hollow carbon decorated with polyaniline for microwave absorption. Chem Eng J 379:122393. https://doi.org/10.1016/j.cej.2019.122393

55. Wu M-Y, Lou Q, Zheng G-S, et al (2021) Towards efficient carbon nanodot-based electromagnetic microwave absorption via nitrogen doping. Appl Surf Sci 567:150897. https://doi.org/10.1016/j.apsusc.2021.150897

56. Qin M, Zhang L, Wu H (2022) Dielectric Loss Mechanism in Electromagnetic Wave Absorbing Materials. Adv Sci 9:2105553. https://doi.org/10.1002/advs.202105553

57. Gu W, Ong SJH, Shen Y, et al (2022) A Lightweight, Elastic, and Thermally Insulating Stealth Foam With High Infrared-Radar Compatibility. Adv Sci 9:2204165. https://doi.org/10.1002/advs.202204165

Graphical abstract